Synchrotron-based investigations of the nature and impact of iron contamination in multicrystalline silicon solar cells

Tonio Buonassisi[a)] and Andrei A. Istratov
Lawrence Berkeley National Laboratory, 1 Cyclotron Road, Berkeley, California 94720 and Electronics Research Laboratory, Department of Materials Science and Engineering, University of California, Berkeley, California 94720

Matthias Heuer
Lawrence Berkeley National Laboratory, 1 Cyclotron Road, Berkeley, California 94720 and University of Leipzig, Scharnhorststrasse 20, D-04275 Leipzig, Germany

Matthew A. Marcus
Advanced Light Source, Lawrence Berkeley National Laboratory, 1 Cyclotron Road, Berkeley, California 94720

Ralf Jonczyk
GE Energy, 231 Lake Drive, Newark, Delaware 19702

Joerg Isenberg
Fraunhofer Institute for Solar Energy Systems, Heidenhofstrasse 2, D-79110 Freiburg, Germany

Barry Lai, Zhonghou Cai, and Steven Heald
Advanced Photon Source, Argonne National Laboratory, 9700 S. Cass Avenue, Argonne, Illinois 60439

Wilhelm Warta, Roland Schindler, and Gerhard Willeke
Fraunhofer Institute for Solar Energy Systems, Heidenhofstrasse 2, D-79110 Freiburg, Germany

Eicke R. Weber
Electronics Research Laboratory, Department of Materials Science and Engineering, University of California, Berkeley, California 94720 and Lawrence Berkeley National Laboratory, 1 Cyclotron Road, Berkeley, California 94720

Synchrotron-based microprobe techniques were used to obtain systematic information about the size distribution, spatial distribution, shape, electrical activity, chemical states, and origins of iron-rich impurity clusters in multicrystalline silicon (mc-Si) materials used for cost-effective solar cells. Two distinct groups of iron-rich cluster have been identified in both materials: (a) the occasional large (diameter ≥ 1 μm) particles, either oxidized and/or present with multiple other metal species reminiscent of stainless steels or ceramics, which are believed to originate from a foreign source such as the growth surfaces, production equipment, or feedstock, and (b) the more numerous, homogeneously distributed, and smaller iron silicide precipitates (diameter ≤ 800 nm, often ≤ 100 nm), originating from a variety of possible formation mechanisms involving atomically dissolved iron in the melt or in the crystal. It was found that iron silicide nanoprecipitates account for bulk Fe concentrations as high as $10^{14}-10^{15}$ cm^{-3} and can have a large negative impact on device performance because of their high spatial density and homogeneous distribution along structural defects. The large (diameter ≥ 1 μm) particles, while containing elevated amounts—if not the majority—of metals, are low in spatial density and thus deemed to have a low direct impact on cell performance, although they may have a large indirect impact via the dissolution of Fe, thus assisting the formation of iron silicide nanoprecipitates. These results demonstrate that it is not necessarily the total Fe content that limits the mc-Si device performance but the distribution of Fe within the material. © *2005 American Institute of Physics.* [DOI: 10.1063/1.1866489]

I. INTRODUCTION

In terms of peak power, over 50% of the worldwide solar cell market is based on multicrystalline silicon (mc-Si).[1] It is known that even minute concentrations [<1 ppb (parts per 10^9)] of iron can drastically reduce the minority-carrier dif-fusion length in p-type silicon, the base material for the vast majority of crystalline silicon photovoltaic (PV) devices. Just $\sim 2 \times 10^{12}$ cm^{-3} of interstitial Fe (Fe$_i$) or $\sim 2 \times 10^{13}$ of iron–boron (Fe$_i$–B$_s$) pairs in single-crystalline silicon can reduce the minority-carrier diffusion length to 50 μm ($\tau \sim 1$ μs), which is lower than the desirable value for most PV devices of reasonable efficiencies.[2] Despite this fact, recent neutron activation analysis (NAA) data on several commercially available mc-Si solar cell materials reveal Fe concentrations

[a)]Author to whom correspondence should be addressed; present address: Lawrence Berkeley National Laboratory, Mail Stop 62R0203, 1 Cyclotron Road, Berkeley, CA 94720; FAX: +1-510-486-4995; electronic mail: buonassisi@alumni.nd.edu

as high as $10^{14}-10^{16}$ cm^{-3}.[3,4] The question naturally arises as to how mc-Si can contain so much iron yet manage to achieve reasonable operating efficiencies. Deep-level transient spectroscopy/microwave photoconductive decay (DLTS/μ-PCD) measurements[5–8] typically reveal only $10^{11}-10^{13}$ cm^{-3} of Fe$_i$ or Fe$_i$–B$_s$ in mc-Si. Hence, the majority of iron should be in agglomerates or precipitates, which are less detrimental to solar cell performance than interstitial iron.

The impact of Fe on device performance is shown herein to depend on the nature and the distribution of Fe contamination in mc-Si, rather than the total Fe concentration. Up until recently, a precise experimental determination of the nature and distribution of Fe had been challenging. Although Fe-rich clusters can have a strong impact on electrical measurements, their small size ($\leqslant$100-nm diameter) renders them undetectable to most macroscopic analytical techniques. In addition, their inhomogeneous spatial distribution and relatively low density can make them difficult to detect in transmission electron microscopy. In contrast, synchrotron-based analytical microprobe tools provide both the sensitivity and the large scanning volumes necessary to detect and characterize multiple nanometer-sized metal clusters within a silicon matrix.[9,10] Since the advent of synchrotron-based analytical microprobe techniques, there have been reports of Fe-rich clusters in a variety of mc-Si materials,[4,9–14] yet little effort has been invested into systematically characterizing these clusters and drawing meaningful physical trends from the data.

In this study, synchrotron-based microprobe techniques were used to systematically characterize iron-rich precipitates and inclusions affecting two very different types of mc-Si solar cell materials: directionally solidified cast mc-Si and AstroPower SiliconFilm™ sheet material. Directionally solidified mc-Si material[15] can take days to cool down after being casted in a typical 200–300-kg ingot. SiliconFilm™ sheet material[16–18] is grown by a different process, involving lower-quality feedstock and high crystal-growth rates, which produces 600–800-μm-thick sheets of mc-Si material. A typical cooling time from the silicon melting point to room temperature is measured in minutes. While such a high throughput, low-cost process has the potential to significantly reduce the price of PV,[19] it also results in higher densities of structural defects[20] and increased impurity content in the material, including carbon- and oxygen-related defects[6,18] and transition metals.[4,18] Through the analysis of Fe-rich inclusions and precipitates in both cast and sheet mc-Si materials, certain trends were observed, which elucidate the origins of iron contamination, the mechanisms for incorporating large amounts of Fe into mc-Si, quantitative information about the distribution of Fe in mc-Si, and the impacts of such contamination on solar cell performance.

II. MATERIALS AND METHODS

The sheet material used in this study was provided by AstroPower, out of which samples of approximately 1 $\times$ 2 cm^2 were extracted. Cast mc-Si wafers, grown by a commercial supplier, were cut from both vertical and hori-
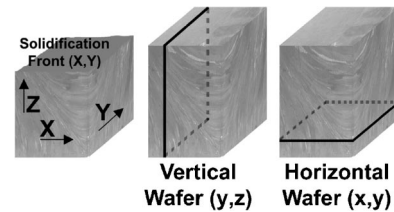

FIG. 1. Pictorial representation of the cast multicrystalline silicon ingot. Z coordinate depicts the crystal-growth direction; X-Y plane represents the solidification front. From this ingot, vertical (middle) and horizontal (right) wafers can be extracted.

zontal slices of the ingot, as depicted in Fig. 1. Some of these wafers were fabricated into solar cells and characterized by laser-beam induced current (LBIC) at the Fraunhofer Institute for Solar Energy Systems in Freiburg, Germany. Regions of interest towards the bottom of the ingot were selected because of the low LBIC signal indicating poor material performance. Samples approximately 1×1 cm^2 were extracted from these regions of interest in the processed wafers. Similar samples were also extracted from these same locations in the unprocessed sister wafers (i.e., wafers extracted from neighboring slices of the ingot). The metallization and antireflection coating were removed, and all samples were slightly etched to remove possible surface contamination.

The synchrotrons utilized throughout this study are the Advanced Photon Source (APS) at Argonne National Laboratory, and the Advanced Light Source (ALS) at Lawrence Berkeley National Laboratory. Specifically, ALS beamlines 10.3.1 (Ref. 21) and 10.3.2 (Ref. 22), and APS beamlines 2-ID-D (Refs. 23 and 24) and 20-ID-B (Ref. 25) were employed in these investigations. At these beamlines, state-of-the-art analytical x-ray microprobes can achieve spot sizes of 200 nm–5 μm in diameter. A small beam size, high flux, and ultralow bremsstrahlung background allow one to achieve the high sensitivity necessary to detect very small metal clusters. On the other hand, given a typical accumulation time at each spot on the order of a second, only small areas of a sample (typically from several hundreds to several thousands of μm^2) can be mapped if a step size comparable to the beam size is used. Since the area of a solar cell is much larger, one has to use a complementary technique to identify the underperforming regions of the cell for further investigation. This can be done by a large, undersampled (i.e., with a step size much larger than the x-ray beam spot size) maps of the recombination activity taken *in situ* by the x-ray beam induced current (XBIC) technique,[13] which is comparable[14] with the LBIC technique.

After a region of interest in the sample is identified by XBIC, x-ray fluorescence microscopy (μ-XRF) scans are performed with a much smaller step size to search for metal-rich clusters embedded in the silicon matrix. The detection limit of the μ-XRF technique is dependent upon the spot size, accumulation time, and overall bulk sensitivity of the system, which can depend on the detector, x-ray flux, and geometry of the system.[26] The total number of Fe atoms

contained within one precipitate (N_{Prec}) located near the sample surface can be determined via the following equation:

$$N_{Prec}(\text{atoms}) = \frac{C_{Prec}(\text{cts/s})}{C_{Std}(\text{cts/s})} \{[\text{Fe}]_{Std}(\text{g/cm}^2)\}$$
$$\times [D_{Std}(\text{atoms/g})][A(\text{cm}^2)]. \quad (1)$$

C_{Prec} and C_{Std} correspond to the measured XRF Fe $K\alpha$ counts, normalized to acquisition time, for the precipitate of interest and standard sample, respectively. $[\text{Fe}]_{Std}$ is the areal Fe density in the standard material, which is typically a NIST 1833 foil for x-ray fluorescence calibration, provided by the National Institute of Standards and Technology (NIST). D_{Std} represents the number of Fe atoms per unit mass of standard material. A is the full width at half maximum (FWHM) of the x-ray beam spot size. Additional corrections (not shown here) may be introduced to account for the depth of the precipitate from the sample surface, and for the flare, i.e., the percentage of x rays falling outside of the FWHM.

To convert N_{Prec} into more meaningful quantities, such as the radius of the precipitate (R_{Prec}, assuming a spherical geometry), the following equation is used:

$$R_{Prec}(\text{cm}) = \left[\frac{3}{4\pi} \frac{N_{Prec}(\text{atoms})}{D_{Prec}(\text{atoms/cm}^3)} \right]^{1/3}, \quad (2)$$

where D_{Prec} is the density of the compound (e.g., $FeSi_2$, Fe_2O_3, etc.) composing the precipitate, in terms of Fe atoms per unit volume.

For typical experimental conditions with a 200-nm-diameter beam and an accumulation time of 1 s, we have detected iron silicide clusters with radius of 23±5 nm, while the noise-limited detection limit for the same conditions was estimated to be 16±3 nm for Fe particles near the sample surface. Because the Fe $K\alpha$ fluorescence at 6.4 keV decays exponentially within the silicon matrix with an attenuation length (decay constant) of approximately 36μm, the sensitivity of μ-XRF decreases for particles embedded deeper within the sample. The depth of the particles from the sample surface can be determined and taken into account during calculations of the particle size by either performing a rotation experiment[27] or by comparing the relative amplitudes of the Fe $K\alpha$ and Fe $K\beta$ peaks in the fluorescence spectra. The latter technique utilizes the fact that Fe $K\alpha$ and Fe $K\beta$ emissions have different energies (6.4 and 7.06 keV, respectively), and thus different attenuation lengths (36 and 48 μm, respectively). Particles within one attenuation length from the surface of the sample are easily detected. High-resolution μ-XRF measurements can also elucidate the morphology of these metal-rich clusters, provided that they are comparable to or larger than the beam spot size.

After metal-rich clusters of interest are located via μ-XRF, their chemical state is assessed via x-ray absorption microspectroscopy (μ-XAS).[28] By using a monochromator to vary the energy of the x-ray beam with an energy resolution of 1 eV or better, the x-ray absorption spectrum of the iron particle is compared against the absorption spectra of commercially available standard materials such as Fe_2O_3 and $FeSi_2$. Powder particles from the standard materials are se-
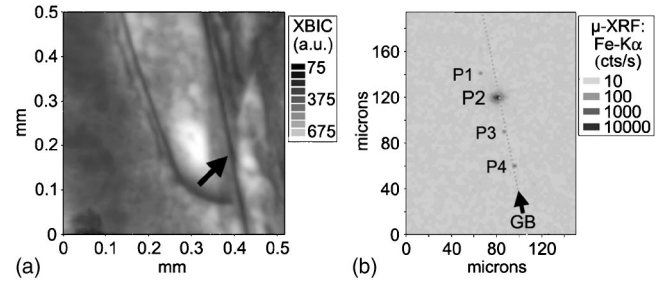

FIG. 2. (a) Typical XBIC image of a cast mc-Si sample extracted from a fully processed vertical wafer (see Fig. 1) near the bottom of the ingot. The arrow in (a) points to a recombination-active grain boundary, a region of which was analyzed by μ-XRF in (b). Fe-rich clusters are found along the grain boundary, highlighted by the arrow and the dotted line in (b). Properties of the Fe-rich clusters labeled "P1"–"P4" are summarized in Table I. Note the log scale of the μ-XRF Fe $K\alpha$ signal intensity, indicating that P2 has approximately two orders of magnitude higher counts than the others.

lected to be comparable to or smaller than the beam spot size, in order to avoid overabsorption and hole effects when measuring the μ-XAS spectra in fluorescence and transmission modes, respectively.[29]

By using this suite of x-ray microprobe analytical techniques, the recombination activity, spatial distribution, elemental composition, size, morphology, and chemical state of iron-rich nanoclusters in silicon can be studied *in situ* with a submicron spatial resolution.

III. RESULTS: CAST mc-Si MATERIAL

XBIC maps reveal certain grain boundaries with exceptionally high recombination activity in both processed [Fig. 2(a)] and unprocessed [Fig. 3(a)] material. Multiple iron-rich clusters are detected by μ-XRF at these locations, as the maps in Figs. 2(b) and 3(b) demonstrate. These iron-rich clusters populating grain boundaries can be divided into two distinct types, with distinct physical properties. Firstly, while the vast majority of iron-rich clusters are small [e.g., P1, P3, and P4 in Fig. 2(b), and all particles in Fig. 3(b)], some rare clusters have nearly two orders of magnitude higher μ-XRF Fe counts [e.g., P2 in Fig. 2(b); note the log scale of Fe concentration]. An analysis by μ-XAS reveals that the clusters with smaller Fe counts are composed of iron silicide ($FeSi_2$), while the clusters with much larger Fe counts are composed of oxidized iron (Fe_2O_3), as shown in Figs. 4(a) and 4(b), respectively.
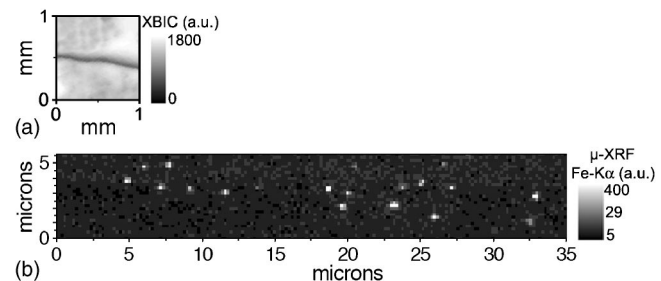

FIG. 3. (a) Large area XBIC and (b) high-resolution μ-XRF map of the iron distribution at a grain boundary in as-grown cast mc-Si. Several $FeSi_2$ nanoprecipitates are observed. Although some clustering is evident on a micron scale, on a larger scale these $FeSi_2$ nanoprecipitates are distributed rather homogeneously.
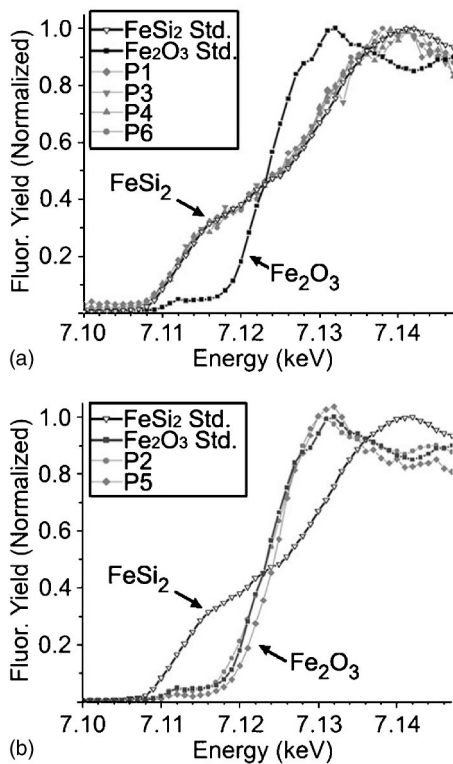
FIG. 4. μ-XAS data discern two types of Fe-rich cluster in cast mc-Si material: (a) smaller iron silicide ($FeSi_2$) and (b) larger iron oxide (Fe_2O_3). Data labels (P1, P2,…) correspond to precipitates viewed in the μ-XRF image, Fig. 2(b), and parameterized in Table I.
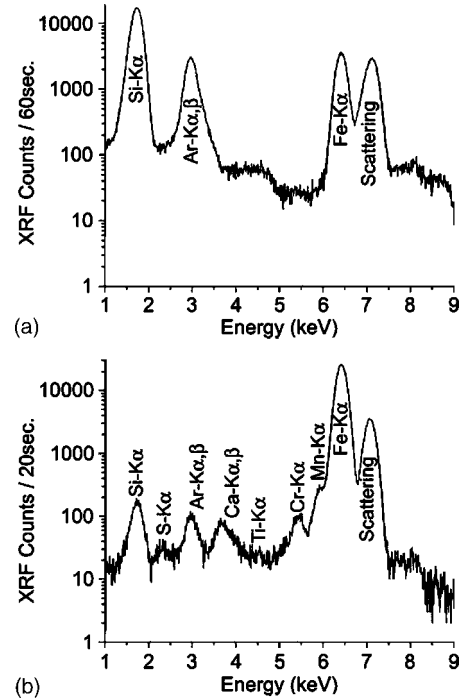

FIG. 5. Typical μ-XRF point scans for the two types of Fe-rich cluster in cast mc-Si: (a) Smaller $FeSi_2$ clusters, without detectable quantities of other metals, and (b) larger Fe_2O_3 particles, wherein iron is accompanied by other elements reminiscent of ceramics, dirt, and furnace components.

The average sizes of these two types of iron-rich cluster, tabulated in Table I indicate that the $FeSi_2$ clusters are indeed smaller than the Fe_2O_3 clusters, as their relative μ-XRF Fe count rate in Fig. 2(b) would suggest.

The compositions of these clusters also differ, as determined by the μ-XRF point scans. While the Fe_2O_3 clusters show appreciable amounts of other contaminants such as Cr, Mn, and Ca [Fig. 5(b)], the smaller $FeSi_2$ clusters show none of these above the μ-XRF detection limit [Fig 5(a)]. Only in

as-grown material can Ni and Cu be found precipitated in the immediate vicinity of $FeSi_2$ in detectable quantities, but not Cr, Mn, Ti, or Ca.

Additionally, the morphologies and orientations of these two types of cluster are very distinct. The large Fe_2O_3 clusters do not appear to be preferentially oriented along the grain boundary or the crystal-growth direction, as evidenced by the nearly symmetric values of their spatial dimensions given in Table I. However, the $FeSi_2$ particles are elongated along the grain boundary only in the direction of the crystal growth, by a factor of at least 3–4, as reported in Table I and depicted graphically in Fig. 6. (Note that a spatial dimension in Table I of 200–300 nm corresponds to the diameter of the beam, indicating that these values may, in fact, be much smaller.) The possible nature of these elongated $FeSi_2$ particles is discussed in Sec. V B.

The distributions of these clusters also differ. While the large Fe_2O_3 clusters are inhomogeneously distributed, the smaller $FeSi_2$ clusters appear to be more regularly spaced. While high-resolution μ-XRF maps [i.e., Fig. 3, showing (a) XBIC and (b) μ-XRF maps along a recombination-active grain boundary of an as-grown horizontal wafer] typically show some microscopic clustering among $FeSi_2$ nanoprecipitates, on a length scale of hundreds of microns, these nanoprecipitates are fairly regularly spaced. Taking into account the attenuation length of the Fe $K\alpha$ fluorescence in Si, one calculates a $FeSi_2$ precipitate density of $(1.5-2) \times 10^6/cm^2$ of grain-boundary surface area in Fig. 3, resulting in an average spacing between precipitates of $7-8$ μm along the grain boundary. The typical number of iron atoms in each of these nanoprecipitates at the grain boundaries was determined, by comparison with standard material and use of Eq. (1), to be $(2.9-3.6) \times 10^6$.
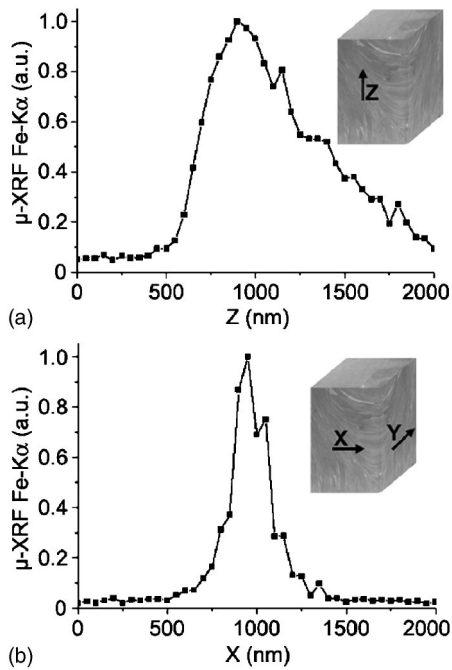
TABLE I. Dimensions and chemical states of various Fe-rich clusters detected by μ-XRF along a strongly recombination-active grain boundary in cast mc-Si material. Dimensions X and Y are perpendicular to the crystal-growth direction of the directionally solidified cast multicrystalline silicon ingot, while Z is parallel to the growth direction, as shown by Fig. 1 and the insets in Fig. 6. Dimensions were determined by the full width at half maximum of the Fe concentration extracted from high-resolution μ-XRF line scans, while chemical states were measured with μ-XAS. Notice the elongation of $FeSi_2$ clusters along the crystal-growth direction (Z dimension). Clusters P1–P4 are shown in Fig. 2(b), and the line scans across P3 are shown in Fig. 6. Note also that the beam spot size is roughly 200 nm, thus dimensions given as 200–300 nm may in reality be much smaller.

Cluster label	Chemical state	X diameter (nm)	Z diameter (nm)
P1	$FeSi_2$	290	547
P2	Fe_2O_3	1250	892
P3	$FeSi_2$	$\leqslant 200$	710
P4	$FeSi_2$	275	772
P5	Fe_2O_3	~ 1450	~ 1800
P6	$FeSi_2$	$\leqslant 200$	570

FIG. 6. High-resolution μ-XRF line scans across an FeSi$_2$ nanoprecipitate at a grain boundary in cast mc-Si with 200-nm beam size and 50-nm step size. The Z dimension corresponds to the crystal-growth direction of the cast multicrystalline silicon ingot, while X and Y are perpendicular to the growth direction, as shown in Fig. 1. While these particles appear thin and symmetric in the dimensions of X [shown in (b)] and Y (not shown), indicating that in these dimensions the particle is equal to or smaller than the beam spot size of 200 nm, the Z dimension (along the growth direction) shows a rather abrupt increase followed by a tailing off of the Fe concentration. A possible formation mechanism for these FeSi$_2$ nanoparticles is discussed in Sec. V B.

IV. RESULTS: SHEET MATERIAL

As only the metal clusters that remain after device processing directly affect the performance of the solar cell device, a sample from as-grown sheet material was subject to an aluminum gettering sequence for 4 h at 800 °C to simulate intense processing. A coarse XBIC scan (Fig. 7) over the front surface (the side opposite to the growth substrate and aluminum layer, i.e., closer to the hypothetical p-n junction, were this material to be fabricated into a solar cell) of the sheet material sample reveals two prominent features of low minority-carrier diffusion length that have persisted despite the Al gettering treatment: (a) strongly recombination-active grain boundaries, appearing as dark lines in Fig. 7, and (b) localized intragranular defects, appearing as dark dots within the grains of Fig. 7.

μ-XRF point spectra (not shown) reveal Fe present at both these locations, with a small contribution from Cr in the case of certain intragranular defects. High-resolution μ-XRF maps reveal that the intragranular defects are irregular in shape and consist of an agglomeration of many nanoparticles, as shown in Figs. 8(a) and 8(b). In the spaces between intragranular defects, where the XBIC signal is higher, no Fe-rich particles are detected. These intragranular defects may consist of iron precipitated at voids and their associated dislocation bunches, which are known to exist in this material.[18,30] The grain boundaries are also decorated by Fe-rich nanoparticles, as shown in Fig. 8(c). The chemical states
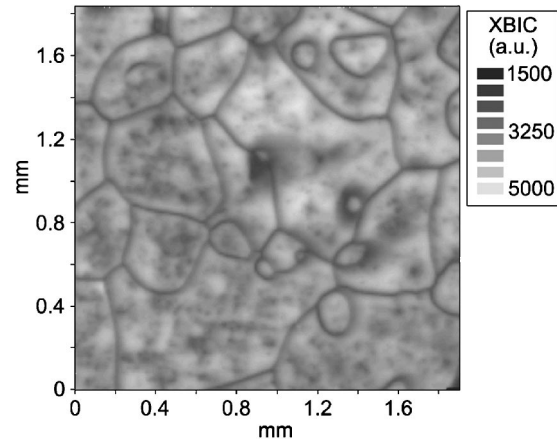

FIG. 7. XBIC map of a typical region of Al-gettered sheet material. Features of interest include recombination-active grain boundaries and pointlike intragranular defects. The dark regions in the map correspond to the areas with high recombination activity.

of these particles were measured by μ-XAS; by comparison with standard material, it is deduced that Fe is most likely to be in the form of iron silicide, as shown in Fig. 8(d).

Like in cast material, the spacing and average size of the iron silicide precipitates along the grain boundaries of this material were significantly homogeneous. The particle density along the surface of the grain boundary was determined to be within the range of $(1-2) \times 10^7$ cm^{-2}, by counting the number of particles in the μ-XRF image of Fig. 8(c) and considering the extinction distances of incoming and outgoing x-rays in Si, yielding an average spacing of $2-3$ μm between neighboring particles. (Note that this value for the particle density along grain boundaries is consistent with the
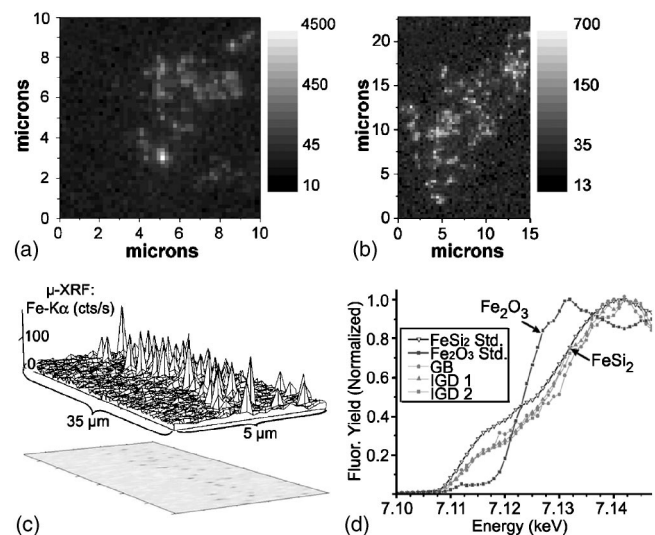

FIG. 8. (a, b) μ-XRF maps of the Fe distribution within typical intragranular defects in sheet material, noted by points of lower XBIC signal in Fig. 7. These defects consist of irregularly shaped, micron-sized clusters of Fe nanoprecipitates. (c) μ-XRF map of Fe nanoprecipitates (radii $\sim 23 \pm 5$ nm) within a typical grain boundary, shown in three-dimensional (3D) (above) and in two-dimensional (2D) projections (below). Despite the small size of individual Fe nanoprecipitates, they are estimated to contain a considerable fraction of the total Fe content in this sample due to their high spatial density (see Table II). (d) The chemical state of the Fe nanoparticles shown in (a-c) is revealed by μ-XAS to be most similar to FeSi$_2$.
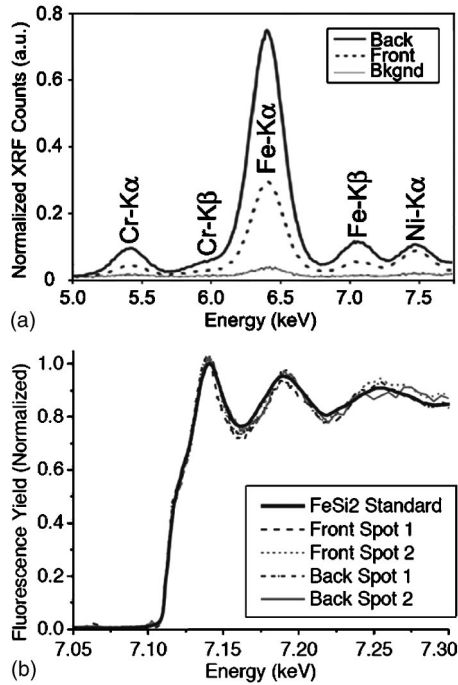
FIG. 9. (a) Time-normalized μ-XRF point spectra of Cr/Fe/Ni-rich particles in the front and back sides of an as-grown sheet material sample. The similar composition of these particles is noted, although the particle on the back surface yields a larger XRF signal, indicating more metals are present. (b) The chemical state of the Fe in such particles found on both the back and front surfaces of the sample is revealed by μ-XAS to be $FeSi_2$. The coincidence of these three metals in the observed proportions suggests contamination by stainless steel; one can conclude from the μ-XAS spectra that these particles were likely introduced in a metallic form, and not as oxides.

FIG. 10. High-resolution μ-XRF mapping reveals the Fe, Ni, and Cr distributions at a large defect cluster in the as-grown sheet material. The entire defect cluster spans many tens of microns, with a few hundred microns between clusters. Because of the low spatial densities, such clusters are deemed to have a relatively small direct impact on device performance. However, they may have a large indirect effect, via the dissolution of Fe and formation of many smaller, more distributed $FeSi_2$ nanoprecipitates. Thus it is not the total metal content, but its distribution, that can limit the material performance.

value of 2×10^7 cm^{-2} obtained by Lu *et al.*[6] on a similar sample via etch pit counting.) The average iron content of each of these precipitates at the grain boundaries was determined, by comparison with standard material and use of Eq. (1), to be $(0.69–2.1) \times 10^6$ Fe atoms. Per Eq. (2), this would correspond to a radius of 23 ± 5 nm, if assumed spherical.

Another sheet material sample—which was not subject to an aluminum gettering treatment—was etched severely, removing 25 μm from the front and back surfaces. Large metallic clusters consisting of Fe, Ni, and Cr could be detected on both sides of the sample by μ-XRF. Large areas $(1 \times 2$ mm$^2)$ of the front and back surfaces were scanned with μ-XRF with a spot size of 5×7 μm^2, so as to determine the spatial density of the intragranular defects. It was found that while the relative composition of these particles remains largely the same (see Fig. 9), their spatial densities are remarkably different. While towards the back surface of the wafer (the side facing the substrate and the last to crystallize) nearly 30 such particles were observed within the 1 $\times 2$ mm^2 scan area, towards the front surface (the side facing away from the substrate and the first to crystallize), less than 10 were detected. In addition, the clusters detected on the front side appeared less strongly in μ-XRF mapping, indicating lower impurity concentrations. This can also be observed when comparing time-normalized μ-XRF point spectra [Fig. 9(a)]. It is also worth noting that the relative concentrations of the three metals shown in Fig. 9(a) (Cr, Fe, and Ni) are nearly the same as those reported in NAA analyses[4] on this material.
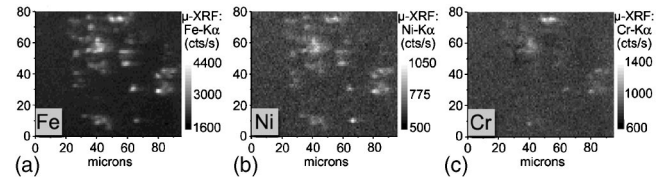
The morphology of these (Cr+Fe+Ni)-rich clusters becomes evident through higher-resolution μ-XRF mapping. Shown in Fig. 10 is a high-resolution image of one such cluster near the rear surface of the sample. The clusters typically consist of various smaller particles, each measuring some $<2–5$ μm in diameter, which are agglomerated in loosely packed clusters measuring up to $50–100$ μm across. μ-XAS measurements on at least five of these clusters indicate that Fe is present as $FeSi_2$, as shown in Fig. 9(b).

It must also be mentioned that one Fe-rich cluster identified by μ-XRF mapping deviates significantly from the others in terms of morphology, composition, and chemical state. This large Fe-rich particle detected near the rear surface of the as-grown sample measures up to 25 μm in diameter [Fig. 11(a)], and contains no Cr nor Ni above the detection limit. In addition, the μ-XAS spectrum of this particle clearly indicates the presence of Fe_2O_3 [Fig. 11(b)]. The overall density of these particles is believed to be rather low, given the sighting of only one such particle in a scan area of several mm^2.

To summarize, in these sheet material samples, two distinct classes of Fe-rich particles have been observed: (1) iron silicide nanoprecipitates, present in higher densities at the grain boundaries and intragranular defect clusters, and (2) a lower density of micron-sized particles, either consisting of elements suggestive of stainless steel (Fe+Cr+Ni) or oxidized iron.
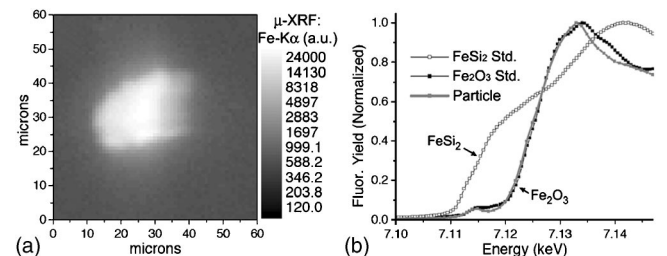

FIG. 11. (a) μ-XRF and (b) μ-XAS of an oxidized iron particle in an as-grown sheet material. Note the large size of this particle relative to the iron silicide nanoprecipitates [Figs. 3(b) and 8(a)–8(c)]. Such a particle, with a large size and oxidized chemical state, is most likely to be an inclusion.
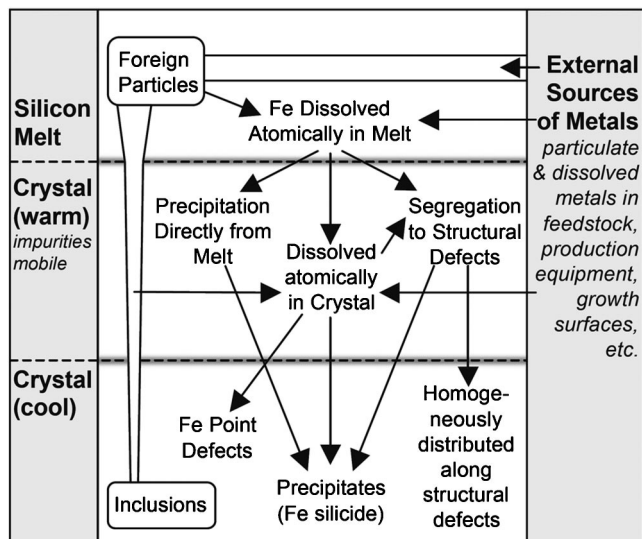
FIG. 12. Graphical representation of Sec. V A–V C, showing the origins of Fe contamination in mc-Si (Sec. V A), the physical mechanisms responsible for incorporating large amounts of Fe into the mc-Si material when warm, i.e., temperatures at which impurity atoms are mobile (Sec. V B), and the formation mechanisms of the Fe-rich clusters one observes in finished mc-Si material (Sec. V C). Two types of Fe-rich cluster are observed in the finished material: inclusions of foreign particles introduced into the melt, and iron silicide nanoprecipitates formed from dissolved iron. Note that the partial or complete dissolution of the former can contribute to the formation of the latter.

V. DISCUSSION

A. Origins of metal contamination in mc-Si

Based on experimental evidence herein and on other reports in the literature, one deduces that the origins of metals in most mc-Si materials likely include some combination of the following: metals dissolved in the silicon feedstock, foreign metallic particles introduced with the feedstock, metals originating from furnace or production equipment, and metals diffusing from the walls of the crucible or growth surfaces. Figure 12 presents a pictorial summary of these processes. As indicated by the arrows emanating from the right-hand side of Fig. 12 and into the melt and warm crystal, metals can be introduced at various stages of the mc-Si crystal-growth process. The following paragraphs explore the experimental evidence that leads to these conclusions.

The hypothesis that foreign particles (originating from the feedstock, production equipment, etc.) are incorporated into the melt is substantiated by the μ-XRF observations of a few metal-rich particles of unusually large sizes [typically ≥ 1 μm, see Figs. 10 and 11(a), and Table I]. All of these large particles observed have one or both of the following additional characteristics: (a) the coincidence of iron with large amounts of other (often slowly diffusing) metal species (e.g., Ca, Ti, Cr, Mn, Ni, etc.), the relative proportions of which allude to certain steels or ceramics [e.g., Figs. 5(b), 10, and 9(a)]and (b) an oxidized chemical state [e.g., Figs. 4(b) and 11, and Table I].

This last point is a significant indicator of foreign particles being included in the melt, as it is currently believed that oxidized iron compounds are not thermodynamically favored to form under equilibrium conditions within silicon,

since the iron–oxygen binding energy is much weaker than that of silicon–oxygen, and thus iron cannot "out-compete" silicon for the oxygen.[31] (For additional discussion regarding the formation of oxidized metal compounds in Si, see Ref. 32.) However, an Fe_2O_3 particle inserted into the silicon melt should retain its structural integrity for a limited time, as the melting temperature of Fe_2O_3 is approximately 1565 °C, about 150 °C above the melting temperature of Si. Nevertheless, because molten Si is a reactive environment, it is extremely likely that these particles will, over time, be etched away by the melt and lead to the formation of smaller, more distributed iron silicide particles.

If a limited amount of iron dissolves from iron oxide particles, then it is likely that an even greater amount of iron should dissolve from large metallic iron and iron silicide particles, given that (a) the melting temperatures of iron–silicon alloys are below that of silicon,[33] and (b) the binding energy of iron atoms to a metallic iron or an iron silicide particle is weaker than to an iron oxide particle.[9] The large, micron-sized (Fe+Cr+Ni)-rich clusters observed by μ-XRF in sheet material (Fig. 8), the compositions of which are very similar to stainless steel [Fig. 9(a)], were determined by μ-XAS to be composed of $FeSi_2$ [Fig. 9(b)]. One can conclude that this iron was most likely introduced into the melt as metallic stainless-steel particles, given that oxide particles are expected to survive the rapid crystallization process. It thus seems very plausible that Fe can dissolve from the micron-sized, unoxidized (Fe+Cr+Ni)-rich clusters during crystal growth and subsequent processing, contaminating nearby structural defects.

The inclusions of large particles show variations in their chemical and elemental compositions, indicating a variety of origins. These particles may originate from the feedstock or furnace parts, as suggested by the observations of stainless-steel inclusions. However, those are not the only possible sources of iron. Recent results by Rinio *et al.*[34] suggest that Fe diffuses in from the walls of the casting crucible after the cast mc-Si crystal has solidified but before it has cooled. It must be remembered that iron is present in the silicon nitride crucible lining typically in concentrations as high as ppm. Impurities likely diffuse not only into the finished crystal but also into the melt, thereby raising the Fe content of the melt and contributing to $FeSi_2$ nanoprecipitate formation.

While impeding the introduction of metals into the melt via the feedstock, production equipment, and/or growth surfaces will undoubtedly lead to improved materials, often there are certain limits imposed by economics, materials suppliers, or crystal-growth conditions. Other strategies must be developed in parallel to limit the impact of metals on device performance. These require an understanding of how large amounts of metals are incorporated into mc-Si, how metal-rich clusters are formed, and how their distribution impacts the electrical properties of the material.

B. Incorporation of large amounts of Fe into mc-Si

As shown in Fig. 12, there are (at least) five pathways for incorporating Fe into the warm mc-Si material: (a) direct incorporation of incompletely dissolved foreign metal-rich

particles into the crystal as inclusions, (b) direct precipitation of locally supersaturated iron from the melt, (c) segregation of metals dissolved in the melt to structural defects, (d) incorporation of dissolved Fe in the melt into single-crystalline regions of the material as Fe_i, and (e) diffusion of Fe from the growth surfaces into the solidified, but still warm, crystal.

The latter two mechanisms (d and e) are rather limited in their potential to introduce large amounts of Fe into most mc-Si materials. Mechanism (e) only affects the border regions of the crystal.[34] For ribbon or sheet materials only fractions of a millimeter thick, however, this may be a motive of concern as the impurity species is more likely to diffuse through the entire thickness of the material. As far as mechanism (d) is concerned, simple equilibrium segregation models alone cannot account for the fact that $10^{14}-10^{16}$ cm^{-3} Fe (Ref. 4) is present in mc-Si materials. Were the amount of Fe incorporated into the final crystal determined simply by the segregation of iron from the melt into single-crystalline regions (as defined by $k_{Si}=8\times10^{-6}$, i.e., the ratio of Fe solubilities in the melt and in single-crystalline silicon, from Ref. 35), this would imply that the melt at the solid-liquid interface contained as much as 0.01%–1% Fe! If, in fact, this much Fe were present, instability in the solid-liquid interface would arise, and certainly columnar crystal growth with centimeter-sized grains would not proceed as desired in the case of cast mc-Si.

The first three mechanisms described in the first paragraph of this section (mechanisms a, b, and c) can account for large amounts (parts per billion/million) of iron being incorporated into mc-Si. Evidence for mechanism (a), the inclusion of foreign particles, is provided by the μ-XRF and μ-XAS observations of oxidized iron and suspected stainless-steel particles in the finished material. During crystal growth, foreign particles in the melt can become trapped at interruptions in the solid-liquid interface caused structural defects such as grain boundaries, instead of being pushed forward in the melt by a uniformly advancing solidification front. Faster growth velocities tend to trap larger particles.[36] Thus, stainless-steel and iron oxide inclusions in fast-grown sheet material [Figs. 10 and 11(a)] are typically much larger than those found in slowly grown cast mc-Si [Fig. 2(b), Table I]. Furthermore, the density and average size of suspected stainless-steel particles in sheet material are larger towards the back side (the last to solidify) of the material (Fig. 9), evidence for a so-called "snow plow" effect.[36]

As iron-rich particles in contact with the melt dissolve, the dissolved iron content in the melt increases. Furthermore, as crystal growth progresses, the segregation of metals from solid to liquid silicon causes an increase of the metal content in the melt, more noticeably at the solid-liquid interface (depending on convective flows in the melt).[37,38] When high metal contents are present in the melt, mechanisms (b) and (c), described in the first paragraph of this section, can result in the incorporation of large amounts of iron into the final crystal.

The direct precipitation of iron from the melt [pathway (b)] can only occur in special conditions, namely, when the impurity concentration in the melt reaches a critical level, as to promote the onset of a second phase. It is known that when the convective flows in the melt are not sufficient, the impurity concentration at the solid-liquid interface increases as impurities are rejected from the crystal into the melt. Once the impurity concentration at the interface reaches a critical level, any small perturbation of the interface can result in the precipitation of the metal silicide directly into the crystal.[37,39] While the convective flows within the melt during the casting process are not likely to allow impurities to reach critical levels at the planar interface, this might not be the case near grain boundaries. It is known from the work of Abrosimov *et al.*[40] that a grain boundary reaching the solid-liquid interface causes a localized distortion (dip) to occur at the solid-liquid interface. It is conceivable that impurities within this dip may be more sheltered from the convective flow of the melt, wherein they may be able to reach critical concentrations and precipitate directly. The morphology of iron silicide nanoprecipitates along grain boundaries in cast mc-Si [Fig. 6(a)] indicates an abrupt onset and a gradual decay, which may be an indication that locally supersaturated iron at the solidification front precipitates abruptly and tails off.

The last mechanism [pathway (c)] enabling large amounts of iron to be incorporated into mc-Si is the segregation of metals to structural defects. It is known that the solubility of metals in polysilicon is much higher than in single-crystalline silicon, especially at lower temperatures.[41,42] This can be explained by the interaction of metals with dangling or reconstructed silicon bonds in structural defects (e.g., grain boundaries), as well as the reduction of strain energy from impurities settling in a distorted silicon lattice near the structural defects.[41,43–45] Iron incorporated via this mechanism could either remain homogeneously distributed along grain boundaries, below the detection limit of μ-XRF, or could perhaps diffuse along grain boundaries and form iron silicide nanoprecipitates. This hypothesis is consistent with the observation of $\sim10^{14}$ Fe cm^{-3} distributed as silicide nanoprecipitate along grain boundaries in cast mc-Si, which is the same amount of iron estimated to atomically segregate to the grain boundaries at higher temperatures.[46]

C. Precipitation of dissolved Fe during cooling

During sample cooling, supersaturated dissolved metals tend to precipitate at existing defect clusters or form new ones.[47–49] The actual processes leading to precipitate formation during cooling are complex and not entirely understood, but available data[41] suggest that metals supersaturate faster (i.e., have a stronger temperature dependence of solubility) within the regions of the material with fewer structural defects compared to the regions with elevated amounts of structural defects. Therefore, a strong driving force exists for supersaturated metals within single-crystalline regions to accumulate at the grain boundaries and other structural defects during sample cooling. Initially, the distributions of metals at structural defects may be very homogeneous, as described in the discussion on segregation in Sec. V B. Eventually, however, metals homogeneously distributed in the vicinities of structural defects will also reach critical concentrations, inducing precipitation and leading to the formation of iron silicide clusters. With slow cooling rates and high metal con-

TABLE II. Iron concentration contained in each type of defect, as determined from standard-calibrated μ-XRF maps. The larger clusters (inclusions) could be up to several microns in size. However, these were often found in either very low or variable spatial densities, thus contributing to high (e.g., oxide inclusions in sheet) and widely varying (e.g., stainless-steel inclusions) values of calculated local iron concentrations.

	Local iron concentration (cm^{-3})	
Type of defect	Cast material	Sheet material
Iron silicide nanoprecipitates at grain boundaries [e.g., Figs. 3(b) and 8(c)]	$(1-3)\times 10^{14}$	$(0.4-2)\times 10^{15}$
Iron oxide inclusions [e.g., Figs. 2(b) and 11(a)]	$5.2\times 10^{13}-2.3\times 10^{16}$	$6.4\times 10^{16}-4.1\times 10^{18}$
Stainless-steel inclusions (e.g., Figs. 9 and 10, and Table I)	Not observed	$2.3\times 10^{13}-4.2\times 10^{17}$
Iron silicide nanoprecipitates at intragranular defect clusters [e.g., Fig. 8(a) and 8(b)]	Not calculated	$(0.1-3)\times 10^{16}$
Total average iron content[a]	$(4.0-4.7)\times 10^{14}$	$(0.87-1.6)\times 10^{16}$

[a]Total average metal content is determined by neutron activation analysis (Ref. 4) on similar material.

centrations, a few "large" (tens of nanometer diameter) metal silicide precipitates are expected to form. On the other hand, faster cools offer less time for supersaturated metals to diffuse and form large clusters, thus favoring a more homogenous distribution of metals along structural defects, either atomically or as smaller precipitates.[50] This dependence of precipitate size on cooling rate is reflected in the two materials analyzed: cast mc-Si is cooled very slowly and forms relatively larger iron silicide nanoprecipitates with larger spacing in between compared to sheet material, which is grown and cooled comparatively quickly, exhibiting nanoprecipitates of closer spacing and smaller average size despite a total Fe content of one to two orders of magnitude higher than the cast.[4]

D. Estimation of iron concentration in different types of defects

Standard-calibrated μ-XRF data can be used to determine the total amount of metals in iron silicide nanoprecipitates and inclusions of foreign particles.[11,26] The spatial density of such particles can be obtained from μ-XRF maps over large areas. By combining this information, one can determine the local volume concentration of iron contained in different defect types. These data are presented in Table II, for both types of material.

As can be seen in Table II, high local iron concentrations were measured for inclusions of foreign particles. The low and variable spatial densities of such particles often led to high and widely varying local iron concentrations. For example, if one 25-μm-diameter iron oxide particle is detected within a 1×1 mm^2 scan area ($\sim 7.3\times 10^{-5}$ cm^{-3} scan volume), the local Fe concentration is calculated to be as high as 4×10^{18} cm^{-3}! Hence, for iron oxide particles in sheet material, the local iron content measured by μ-XRF within approximately 0.4 mm^3 of material is higher than the NAA values[4] obtained from several hundred mm^3. In other cases, such as stainless-steel inclusions in sheet material, the local iron content varied widely, depending on the location within the material and the distance from the front or back surfaces. Nevertheless, one may conclude with reasonable confidence that the larger inclusions are one of the likely origins for the high metal contents in these materials, contributing both to high NAA measurements and to the formation of other distributions of iron, such as silicide nanoprecipitates and point defects.

A slightly less, but comparable amount of iron is contained in silicide nanoprecipitates. Despite their small size, these particles can be present in very high densities at structural defects, thus accounting for a large fraction of the total iron. Note that all types of cluster detected by μ-XRF contain significantly more iron per unit volume than point defects, determined in comparable material in other studies.[5–8] Nevertheless, concentration comparisons may be somewhat misleading when gauging the total impact of iron on device performance since it is the distribution of iron and not necessarily its total concentration that can have the more severe impact on minority-carrier diffusion length.

E. Impact of iron distribution on minority-carrier diffusion length

The same number of metal atoms can have a large number of unique spatial distributions. By simply changing the distribution of Fe impurity atoms, one can change the volume of material adversely affected by the impurity atoms, and thus, their impact on device performance.[51] This can be understood by considering a hypothetical silicon sample with 10^{14} cm^{-3} of Fe$_i$–B$_s$ or Fe$_i$. The minority-carrier diffusion length in such a sample would be approximately 20 or 10 μm, respectively.[2] Now, let us assume that these iron atoms are allowed to diffuse towards one another and form precipitates of iron silicide. If we approximate the new minority-carrier diffusion length as the distance between neighboring iron silicide clusters, then it is easy to calculate that if the same amount of iron forms precipitates with diameters of 60 nm, the diffusion length would be ~ 30 μm; if the precipitates with diameters of 350 nm form, the average diffusion length would be ~ 180 μm, etc. One can quickly see the pattern: with increasing average precipitate size (and decreasing density of precipitates), the minority-carrier diffusion length increases. It can thus be concluded that it is the distribution of metals and not their total bulk concentration that affects device performance in mc-Si.

Atomically dissolved iron has the highest recombination activity per iron atom, and therefore is the most dangerous state of iron in the solar cell. However, typically only a small fraction of total iron is found in the interstitial or dissolved state. The rest of iron is precipitated. Smaller, more distributed iron silicide nanoprecipitates also have a large impact on cell performance due to the higher total amount of iron in this distribution and the small distance separating adjacent clusters. This is substantiated by the correlation between the recombination-active grain boundaries shown in XBIC images of Figs. 2(a), 3(a), and 7, and the presence of metal silicide precipitates separated by distances of only a few microns [Figs. 2(b), 3(b), and 8(c)]. A model developed by Fedotov *et al.*[52] predicts that when the distance separating neighboring recombination-active clusters along a grain boundary is less than the minority-carrier diffusion length within the grains, the grain boundary becomes noticeably recombination active for minority carriers. This appears indeed to be the case, as the minority-carrier diffusion length within the grains of this region of the sample is determined from LBIC measurements to be >50 μm, while the distance separating neighboring Fe-rich clusters can be as little as a few microns. In addition, recent illuminated lock-in thermography[53] (ILT) or light-modulated lock-in thermography[54] (LimoLIT) measurement techniques developed simultaneously by Fraunhofer ISE and the University of Konstanz, respectively, have indicated that grain-boundary recombination is one of the most dangerous inhomogeneous power-loss mechanisms in mc-Si solar cells operating in 1-sun conditions.[53–55] To improve the solar cell device performance, it is of great interest to understand how to effectively passivate or increase the average distance separating metal-silicide nanoprecipitates as much as possible. Simultaneously, it is desirable that the density of grain boundaries within one minority-carrier diffusion length of the *p-n* junction be as low as possible, a modification only possible in certain materials (e.g., sheet material).

Following similar reasoning, intragranular defects can also have a large negative impact on the minority-carrier diffusion length, which varies with the average distance separating adjacent intragranular defects. This effect can be observed in the XBIC map of Fig. 7, wherein intragranular precipitates [such as those shown in high-resolution μ-XRF in Figs. 8(a) and 8(b)] appear as localized dark points. Areas containing higher densities of these intragranular defects also exhibit lower XBIC signals. As these intragranular defect clusters appear to consist of iron precipitated at the internal surfaces of voids and their surrounding dislocation networks,[18,30] it may be possible to improve material quality by inducing the formation of these voids preferentially towards the back surface of the sample, away from the *p-n* junction.[56]

Much different from the case of iron silicide nanoprecipitates, the micron-sized, isolated iron oxide and stainless-steel inclusions observed in mc-Si material are believed to have a very small *direct* impact on device performance. This is due to the fact that the average distance separating these large metal clusters is often many tens or hundreds of microns, more than the minority-carrier diffusion length in those bad regions. Despite the small direct impact on device performance, these micron-sized metal-rich clusters may have a large *indirect* impact on device performance, provided that metals can dissolve from these clusters and create the smaller, more distributed iron-silicide nanoprecipitates.

VI. SUMMARY AND CONCLUSIONS

Quantitative μ-XRF, in agreement with NAA studies,[3,4] indicates that the majority of iron found in mc-Si is located in metal-rich clusters. The iron-rich clusters detected and analyzed in this study can be divided into two distinct groups: iron silicide nanoprecipitates and micron-sized inclusions. Based on the compositions of these particles, we deduce that the main sources of Fe contamination in mc-Si are iron particles introduced into the melt from the feedstock, growth surfaces, and furnace environment. Some of these particles experience only limited dissolution in the melt and become trapped during crystal growth. These are present in the final material as micron-sized inclusions. Other particles dissolve significantly or completely, contributing to high iron contents in the melt. Iron silicide nanoprecipitates likely form from dissolved iron incorporated into the crystal via segregation to structural defects followed by precipitation, direct precipitation from the melt, or precipitation of dissolved iron inside the crystal.

The impact of metal clusters on solar cell performance strongly depends on their spatial distribution. Homogeneously distributed, recombination-active nanoprecipitates separated by only a few microns have a much greater impact on the minority-carrier diffusion length than micron-sized clusters separated by several hundreds of microns, even if the total amount of iron contained in these two distinct defect types can be comparable. In consequence, it is realized that the iron silicide nanoprecipitates have the greater direct impact on device performance. While the larger, micron-sized Fe-rich clusters and inclusions have a small direct impact on device performance because of their low spatial density, they are believed to have a large indirect impact, since dissolved iron from those larger clusters can contribute to the formation of iron silicide nanoprecipitates. Improvements to solar cell device performance are expected if metals can be engineered into distributions that impact device performance less, namely, by reducing the spatial density of metal-related defects (precipitates and point defects) within one minority-carrier length from the *p-n* junction.

[1] Report IEA-PVPS T1-12:2003, International Energy Agency Photovoltaic Power Systems Programme, 2003.

[2] A. A. Istratov, H. Hieslmair, and E. R. Weber, Appl. Phys. A: Mater. Sci. Process. **70**, 489 (2000).

[3] D. Macdonald, A. Cuevas, A. Kinomura, Y. Nakano, in 29th IEEE Photovoltaic Specialists Conference, New Orleans, LA, 2002 (IEEE, Piscataway, NJ), p. 1707.

[4] A. A. Istratov, T. Buonassisi, R. J. McDonald, A. R. Smith, R. Schindler, J. A. Rand, J. P. Kalejs, and E. R. Weber, J. Appl. Phys. **94**, 6552 (2003).

[5] D. H. Macdonald, L. J. Geerligs, and A. Azzizi, J. Appl. Phys. **95**, 1021 (2004).

[6] J. Lu, M. Wagener, G. Rozgonyi, J. Rand, and R. Jonczyk, J. Appl. Phys. **94**, 140 (2003).

[7] R. A. Sinton, T. Mankad, S. Bowden, and N. Enjalbert, in 19th European Photovoltaic Solar Energy Conference, Paris, France, 2004 7–11 June 2004 (WIP-Munich, Germany and ETA, Florence, Italy), p. 520.

[8] L. J. Geerligs, in *14th Workshop on Crystalline Silicon Solar Cells & Modules: Materials and Processes*, Winter Park, Colorado, USA, 8–11 August 2004 edited by B. L. Sopori (NREL, Golden, CO, 2004), p. 143.

[9] S. A. McHugo *et al.*, J. Appl. Phys. **89**, 4282 (2001).

[10] T. Buonassisi, O. F. Vyvenko, A. A. Istratov, E. R. Weber, Z. Cai, B. Lai, T. F. Ciszek, and R. Schindler, Physica B **340–342**, 1137 (2003).

[11] S. A. McHugo, A. C. Thompson, I. Périchaud, and S. Martinuzzi, Appl. Phys. Lett. **72**, 3482 (1998).

[12] A. A. Istratov, H. Hieslmair, O. F. Vyvenko, E. R. Weber, and R. Schindler, Sol. Energy Mater. Sol. Cells **72**, 441 (2002).

[13] O. F. Vyvenko, T. Buonassisi, A. A. Istratov, H. Hieslmair, A. C. Thompson, R. Schindler, and E. R. Weber, J. Appl. Phys. **91**, 3614 (2002).

[14] T. Buonassisi *et al.*, J. Appl. Phys. **95**, 1556 (2004).

[15] A. Schönecker, L. J. Geerligs, and A. Müller, Solid State Phenom. **95–96**, 149 (2003).

[16] R. B. Hall, A. M. Barnett, S. R. Collins, J. C. Checchi, D. H. Ford, C. L. Kendall, J. A. Rand, and C. B. Moore, US Patent No. 6,111,191 (2000).

[17] J. S. Culik, I. S. Goncharovsky, J. A. Rand, and A. M. Barnett, Prog. Photovoltaics **10**, 119 (2002).

[18] J. Rand, G. A. Rozgonyi, R. Jonczyk, S. Batta, J. Lu, R. Reedy, and R. Zhang, in *12th Workshop on Crystalline Silicon Solar Cell Materials and Processes*, Breckenridge, CO, USA, August 2002 edited by B. L. Sopori (NREL, Golden, CO, 2002), p. 98.

[19] T. Ciszek, in *Crystal Growth Technology*, edited by H. J. Scheel and T. Fukuda (Wiley, Sussex, UK, 2003), p. 267.

[20] G. A. Rozgonyi, J. Lu, R. Zhang, J. Rand, and R. Jonczyk, Diffus. Defect Data, Pt. B **95–96**, 211 (2004).

[21] J. H. Underwood, A. C. Thompson, Y. Wu, R. D. Giauque, K. W. Jones, and M. L. Rivers, Nucl. Instrum. Methods Phys. Res. A **266**, 318 (1988).

[22] M. A. Marcus *et al.*, J. Synchrotron Radiat. **11**, 239 (2004).

[23] Z. Cai *et al.*, AIP Conf. Proc. **521**, 31 (2000).

[24] W. Yun *et al.*, Rev. Sci. Instrum. **70**, 2238 (1999).

[25] S. M. Heald, E. A. Stern, D. Brewe, R. A. Gordon, E. D. Crozier, D. Jiang, and J. O. Cross, J. Synchrotron Radiat. **8**, 342 (2001).

[26] S. A. McHugo *et al.*, J. Cryst. Growth **210**, 395 (2000).

[27] O. F. Vyvenko, T. Buonassisi, A. A. Istratov, and E. R. Weber, J. Phys.: Condens. Matter **16**, S141 (2004).

[28] *X-ray Absorption: Principles, Applications, Techniques of EXAFS, SEXAFS, and XANES*, edited by D. C. Koningsberger and R. Prins (Wiley-Interscience, Eindhoven, The Netherlands, 1988).

[29] A. Manceau, M. A. Marcus, and N. Tamura, in *Applications of Synchrotron Radiation in Low-Temperature Geochemistry and Environmental Science*, edited by P. Fenter and N. C. Sturchio (Mineralogical Society of America, Washington, DC, 2002), p. 341.

[30] R. Zhang, G. Duscher, J. Rand, and G. A. Rozgonyi, in *12th Workshop on Crystalline Silicon Solar Cell Materials and Processes*, Breckenridge, CO, USA, August 2002, edited by B. Sopori (NREL, Golden, CO, 2002), p. 206.

[31] *CRC Handbook of Chemistry and Physics*, 84th ed., edited by D. R. Lide (CRC, Boca Raton, FL, 2003).

[32] T. Buonassisi, M. Marcus, A. Istratov, M. Heuer, T. Ciszek, B. Lai, C. Zhonghou, and E. R. Weber, J. Appl. Phys. (in press).

[33] T. B. Massalski, H. Okamoto, P. R. Subramanian, and L. Kacprzak, *Binary Alloy Phase Diagrams* (ASM International, Materials Park, 1990).

[34] M. Rinio, C. Ballif, T. Buonassisi, and D. Borchet, in 19th European Photovoltaic Solar Energy Conference, Paris, France, 2004 7–11 June 2004 (WIP-Munich, Germany and ETA, Florence, Italy), p. 762.

[35] S. Mahajan and K. S. S. Harsha, *Principles of Growth and Processing of Semiconductors* (WCB/McGraw-Hill, USA, 1999).

[36] D. R. Uhlmann, B. Chalmers, and K. A. Jackson, J. Appl. Phys. **35**, 2986 (1964).

[37] P. S. Ravishankar, J. P. Dismukes, and W. R. Wilcox, J. Cryst. Growth **71**, 579 (1985).

[38] B. Chalmers, J. Cryst. Growth **82**, 70 (1987).

[39] J. P. Kalejs, B. Bathey, and C. Dubé, J. Cryst. Growth **109**, 174 (1991).

[40] N. V. Abrosimov, A. V. Bazhenov, and V. A. Tatarchenko, J. Cryst. Growth **82**, 203 (1987).

[41] R. C. Dorward and J. S. Kirkaldy, J. Mater. Sci. **3**, 502 (1968).

[42] A. A. Istratov, W. Huber, and E. R. Weber, Appl. Phys. Lett. **85**, 4472 (2004).

[43] D. West, S. K. Estreicher, S. Knack, and J. Weber, Phys. Rev. B **68**, 035310 (2003).

[44] A. H. Cottrell and B. A. Bilby, Proc. Phys. Soc., London, Sect. A **62**, 49 (1949).

[45] D. Blavette, E. Cadel, A. Fraczkiewicz, and A. Menand, Science **286**, 2317 (1999).

[46] A. A. Istratov, T. Buonassisi, W. Huber, and E. R. Weber, in *14th NREL Workshop on Crystalline Silicon Solar Cell Materials and Processes*, Winterpark, CO, USA, 8–11 August 2004, edited by B. L. Sopori (NREL, Golden, CO, 2004), p. 230.

[47] W. C. Dash, J. Appl. Phys. **27**, 1193 (1956).

[48] E. Nes and G. Lunde, J. Appl. Phys. **43**, 1835 (1972).

[49] W. T. Stacy, D. F. Allison, and T. C. Wu, J. Electrochem. Soc. **129**, 1128 (1982).

[50] A. A. Istratov, T. Buonassisi, M. A. Marcus, T. F. Ciszek, and E. R. Weber, in *14th NREL Workshop on Crystalline Silicon Solar Cell Materials and Processes*, Winterpark, CO, USA, 8–11 August 2004, edited by B. L. Sopori (NREL, Golden, CO, 2004), p. 165.

[51] P. S. Plekhanov, R. Gafiteanu, U. M. Gosele, and T. Y. Tan, J. Appl. Phys. **86**, 2453 (1999).

[52] A. Fedotov, B. Evtody, L. Fionova, J. Iliashuk, E. Katz, and L. Poljak, J. Cryst. Growth **104**, 186 (1990).

[53] J. Isenberg and W. Warta, J. Appl. Phys. **95**, 5200 (2004).

[54] M. Kaes, S. Seren, T. Pernau, and G. Hahn, Prog. Photovoltaics **12**, 355 (2004).

[55] J. Isenberg and W. Warta, Prog. Photovoltaics **12**, 339 (2004).

[56] S. A. McHugo, E. R. Weber, S. M. Myers, and G. A. Petersen, Appl. Phys. Lett. **69**, 3060 (1996).